

Designed Synthesis and Stacking Architecture of Solid and Mesoporous TiO₂ Nanoparticles for Enhancing the Light-Harvesting Efficiency of Dye-Sensitized Solar Cells

Ji Young Ahn,[†] Kook Joo Moon,[‡] Ji Hoon Kim,[†] Sang Hyun Lee,[§] Jae Wook Kang,^{||} Hyung Woo Lee,[⊥] and Soo Hyung Kim^{*†‡§}

[†]Department of Nanofusion Technology, College of Nanoscience and Nanotechnology, Pusan National University, 30 Jangjeon-dong, Geumjung-gu, Busan 609-735, Republic of Korea

[‡]Department of Samsung Advanced Integrated Circuit, College of Nanoscience and Nanotechnology, Pusan National University, 30 Jangjeon-dong, Geumjung-gu, Busan 609-735, Republic of Korea

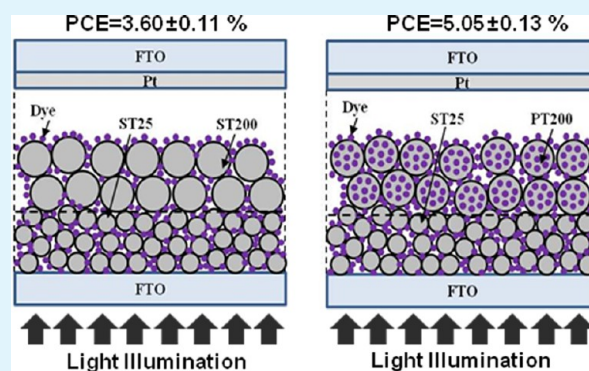
[§]Department of Nanomechatronics Engineering, College of Nanoscience and Nanotechnology, Pusan National University, 30 Jangjeon-dong, Geumjung-gu, Busan 609-735, Republic of Korea

^{||}Department of Flexible and Printable Electronics, Chonbuk National University, 567 Baekje-daero, Deokjin-gu, Jeonju 561-756, Republic of Korea

[⊥]National Core Research Center for Hybrid Materials Solution, Pusan National University, 30 Jangjeon-dong, Geumjung-gu, Busan 609-735, Republic of Korea

ABSTRACT: We fabricated solid and mesoporous TiO₂ nanoparticles (NPs) with relatively large primary sizes of approximately 200 nm via inorganic templates for *aero-sol-gel* and subsequent aqueous-washing processes. The amount of dye molecules adsorbed by the internal pores in the mesoporous TiO₂ NPs was increased by creating the nanopores within the solid TiO₂ NPs. Simultaneously, the light-scattering effect of the mesoporous TiO₂ NPs fabricated by this approach was secured by maintaining their spherical shape and relatively large average size. By precisely accumulating the fabricated solid or mesoporous 200 nm diameter TiO₂ NPs on top of a conventional 25 nm diameter TiO₂ NP-based underlayer, we could systematically examine the effect of the solid and mesoporous TiO₂ NPs on the photovoltaic performance of dye-sensitized solar cells (DSSCs). Consequently, the stacking architecture of the mesoporous TiO₂ NP-based overlayer, which functioned as both a light-scattering and dye-supporting medium, on top of a conventional solid TiO₂ NP-based underlayer in a DSSC photoelectrode (i.e., double-layer structures) was found to be very promising for significantly improving the photovoltaic properties of conventional solid TiO₂ NP single-layer-based DSSCs.

KEYWORDS: *aero-sol-gel process, mesoporous nanoparticles, photovoltaic properties, light-scattering layer, dye-supporting layer*



INTRODUCTION

A dye-sensitized solar cell (DSSC) is a light-harvesting system that is generally composed of a TiO₂ nanoparticle (NP)-accumulated photoelectrode, a redox couple in a liquid electrolyte, and a Pt-coated conducting oxide counter electrode. In the photoelectrode of DSSCs, dye molecules are attached to the surfaces of the TiO₂ NPs. When a DSSC is exposed to sunlight, electrons generated from dye molecules are injected into the conduction band of the TiO₂ NPs and reach the conducting oxide electrode (e.g., fluorine-doped tin oxide, FTO). Then, the photogenerated electrons flow through the external circuit and are reintroduced into the Pt-coated counter electrode, flowing into the liquid electrolyte. The electrolyte finally transports the electrons of a current cycle in DSSCs.^{1–5}

To utilize the incident sunlight efficiently and to improve the photovoltaic properties of DSSCs, many previous approaches

have attempted to employ solid TiO₂ NP-accumulated double layers, which consist of an underlayer of small primary TiO₂ NPs to support the dye molecules and an overlayer of large primary TiO₂ NPs to scatter the incident light.^{6–8} Typically, the light-scattering overlayer is expected to enhance the confinement of the incident light within a photoelectrode, thereby enabling the dye molecules adsorbed on the surface of the TiO₂ NPs to inject more photogenerated electrons. Because the light-scattering efficiency is correlated with the interacting particle size and the wavelength of the incident light,^{9–11} the precise accumulation of solid TiO₂ NPs of different sizes in the photoelectrode is the key for enhancing light harvesting in

Received: September 25, 2013

Accepted: December 30, 2013

Published: December 30, 2013

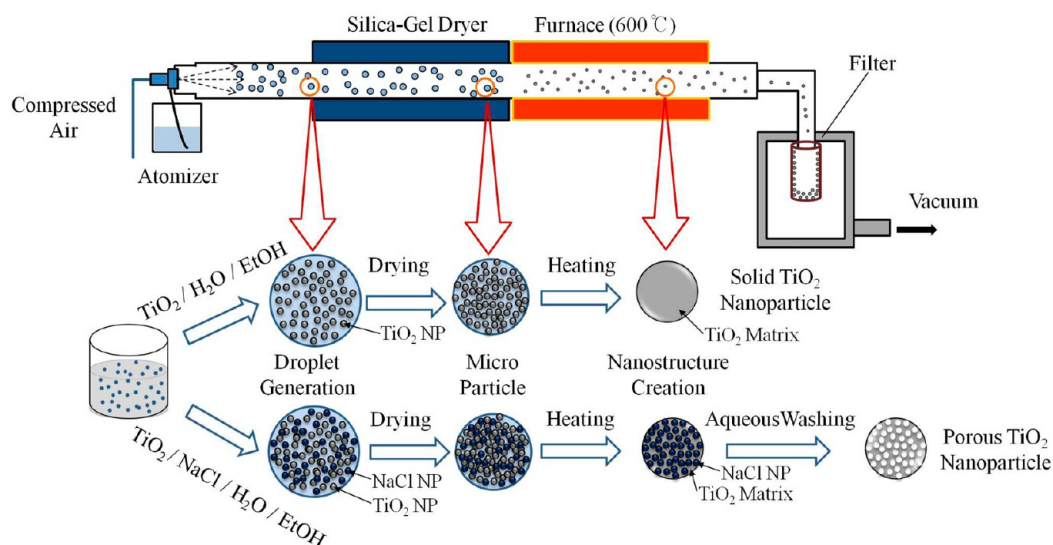


Figure 1. Schematic of fabricating solid and porous TiO₂ nanoparticles via inorganic templates for aero-sol-gel and aqueous-washing processes.

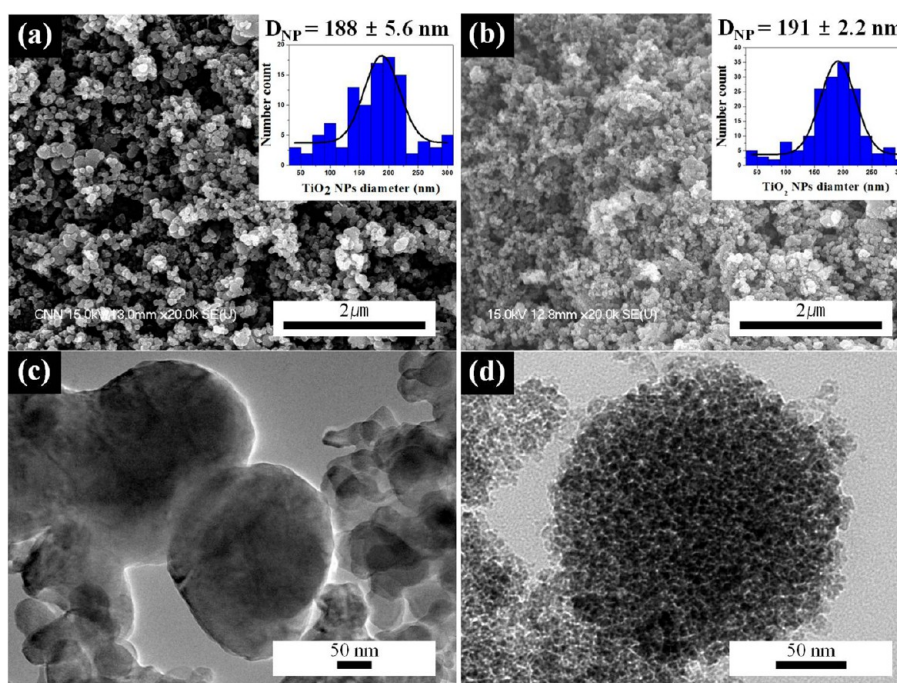


Figure 2. SEM images of (a) solid TiO₂ NPs with an average diameter of 200 nm (ST200) and (b) porous TiO₂ NPs with an average diameter of 200 nm (PT200). TEM images of (c) ST200 and (d) PT200.

DSSCs. Generally, increasing the size of TiO₂ NPs can increase the light-scattering effect; however, it also simultaneously decreases the effective specific surface area needed to support the dye molecules. As an alternative approach, various polymers or inorganic templates have been used to make voids or cracks to secure the available surface area of a TiO₂ NP-accumulated photoelectrode layer.^{12–14} However, those approaches are inherently constrained in terms of increasing the available specific surface area because of limitations on the primary size of solid TiO₂ NPs.

To date, numerous research groups^{9–14} have extensively examined the light-scattering effect of solid TiO₂ NPs on the photovoltaic properties of DSSCs. However, an attempt to use relatively large and highly porous TiO₂ NPs as both a light-scattering and a dye-supporting medium has rarely been made.

In this work, the influence of solid and mesoporous TiO₂ NPs as dye-supporting and light-scattering media on the amount of light harvesting in DSSC photoelectrodes was systematically investigated in terms of open-circuit voltage (V_{oc}), short-circuit current (J_{sc}), fill factor (FF), and power conversion efficiency (PCE).

EXPERIMENTAL DETAILS

Aero-Sol-Gel Synthesis of Solid and Mesoporous TiO₂ NPs.

Figure 1 shows a schematic of the experimental setup for the fabrication of solid and mesoporous TiO₂ NPs by an inorganic template-based aero-sol-gel process.^{15–17} Two types of precursor solutions were made. First, 20 g of inorganic salts (NaCl, Sigma-Aldrich, St. Louis, MO, USA) were completely dissolved in distilled water (90 mL) in a vial (solution 1), and then titanium butoxide (C₁₆H₄₀O₄Ti, 17.15 mL, Sigma-Aldrich, St. Louis, MO, USA) was added to EtOH (72.85 mL) in another vial (solution 2). The two

solutions were then mixed together, and the resulting solution was ultrasonicated for 1 h. This mixed precursor solution was aerosolized by a standard atomizer operated with compressed air at a pressure of 241 kN/m². The micrometer-sized droplets containing tiny TiO₂ NPs were formed by a sol–gel reaction, and solidified particles were continuously formed by passing through a silica-gel dryer via solvent evaporation and adsorption. The solidified aerosol particles composed of TiO₂ and NaCl were then immobilized and sintered by passing through a quartz tube reactor (2.54 cm in diameter × 30 cm in heating length) enclosed by a tube furnace heated at 600 °C. Finally, the resulting TiO₂–NaCl composite NPs were collected in a membrane filter and washed with deionized water. The washing process was repeated more than three times to ensure complete removal of the NaCl templates from the TiO₂–NaCl composite NPs. To fabricate the solid TiO₂ NPs, we followed the same procedure but without employing NaCl (Figure 1).

Fabrication of DSSCs. A TiO₂ NP-accumulated photocatalytic active layer was formed by a screen-printing process on fluorine-doped tin oxide (FTO) glass (SnO₂:F, 7 Ω/sq, Pilkington, Boston, MA, USA) with an active area of 0.6 × 0.6 cm². In previous studies, we experimentally determined that the optimum thickness of a commercial TiO₂ NP-accumulated (Degussa, Germany; hereafter denoted ST25) layer was approximately 20 μm.^{17,18} To prepare the TiO₂ paste for the screen-printing process, 17 g of solid or mesoporous TiO₂ NPs fabricated in this study and 23 g of citric acid dispersed in 29 g of ethylene glycol were mixed in a vial. The TiO₂ NP-accumulated photoelectrode layer was sintered at 500 °C for 30 min and then immersed in 0.5 mM Ru-dye (Bu₄N)₂[Ru(Hdcbpy)₂(NCS)₂] (N719 dye, Solaronix). The photoelectrode layer was immersed for 24 h at room temperature to allow the dye molecules to become attached to the entire surface as well as to the available internal pores of the mesoporous TiO₂ NPs. The dye-soaked TiO₂ NP layer-based photoelectrode was then rinsed with ethanol and dried in a convection oven at 80 °C for 10 min. As a counter electrode, we prepared a Pt-coated FTO glass using ion-sputtering (E1010, Hitachi) operated at 2.5 kV. Both the dye-soaked TiO₂ layer photoelectrode and the Pt-coated counter electrode were then sealed together with an inserted hot-melt polymer film (60 μm thickness, Surlyn, DuPont, Wilmington, DE, USA), and an iodide-based liquid electrolyte (AN-50, Solaronix, Zollikon, Switzerland) was injected into the space between the electrodes.

Characterization of Materials and Photovoltaic Devices. The morphologies of the resulting solid and mesoporous TiO₂ NPs synthesized by the aero-sol–gel process and the fabricated photocatalytic layers were characterized using various techniques, including scanning electron microscopy (SEM; S-4200, Hitachi, Tokyo, Japan) operated at ~15 kV, transmission electron microscopy (TEM; JEM 2100F, JEOL, Tokyo, Japan) operated at ~100 kV, and X-ray diffraction analysis (XRD; Empyrean series 2, PANalytical, Almero, The Netherlands). The specific surface areas of the TiO₂ NPs were calculated with the Brunauer–Emmett–Teller (BET) equation, and their pore-size distributions were determined by using the Barrett–Joyner–Halenda (BJH) formula from the desorption branch. Light reflectance and absorbance of various TiO₂ layers without coating dye molecules were measured using a UV–vis spectrometer (Cary 5000, Agilent, Englewood, CA, USA). The current density–voltage (*J*–*V*) characteristics and impedance spectra of the DSSCs assembled in this study were measured by a solar simulator with an intensity of 100 mW/cm² (PEC-L11, Pecell Technologies, Inc., Yokohama, Japan). The intensity of sunlight illumination was calibrated using a standard Si photodiode detector with a KG-5 filter. The *J*–*V* curves were recorded automatically with a Keithley SMU 2400 source meter (Cleveland, OH, USA) by illuminating the DSSCs. The electrochemical impedance spectroscopy (EIS) measurements for DSSCs were made under the illumination of 100 mW/cm², and the explored frequency range was from 0.0001 to 100 kHz. Here, the bias voltage and ac amplitude were set at the *V*_{oc} of DSSCs and 10 mV, respectively.

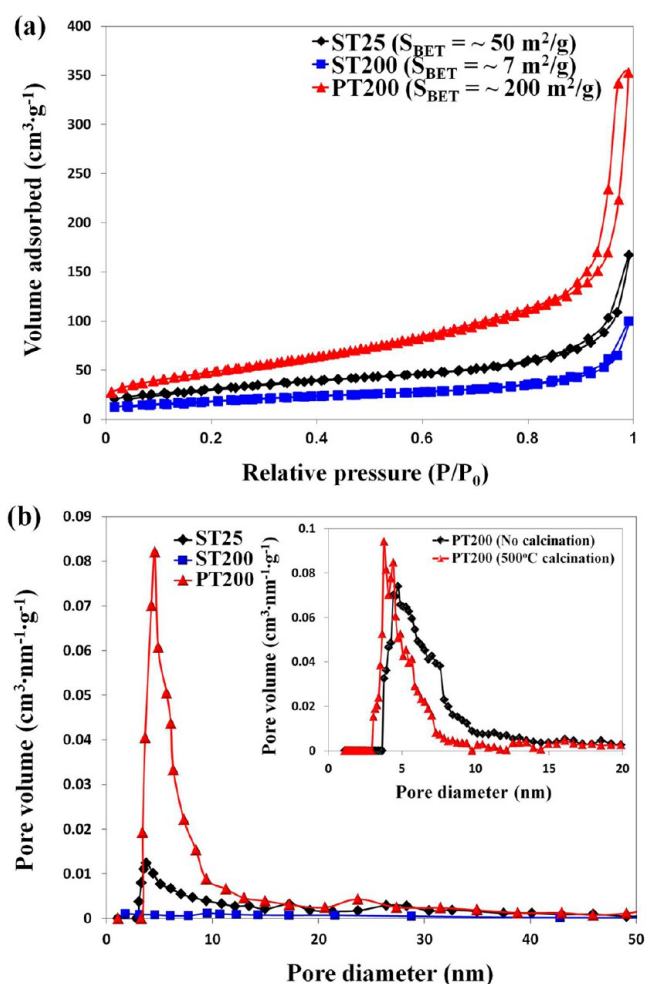


Figure 3. (a) Nitrogen adsorption and desorption of ST25, ST200, and PT200. (b) Pore-diameter distributions of ST25, ST200, and PT200. The inset is the pore-diameter distribution of PT200 before and after calcination at 500 °C.

RESULTS AND DISCUSSION

To examine the structural differences of the as-prepared solid and porous TiO₂ NPs, we performed SEM and TEM analyses. The SEM images in Figure 2a,b show that both the as-prepared solid and the porous TiO₂ NPs were spherical and loosely aggregated; their average diameter was ~200 nm. There were no appreciable differences in either the morphology or the size of the solid and porous TiO₂ NPs. This suggests that the salt templates employed in fabricating the TiO₂–NaCl composite NPs were homogeneously distributed in the TiO₂ matrix. The inorganic salt templates residing inside the TiO₂ NPs played a key role in securing the pore structure for the porous TiO₂ NPs before the aqueous salt removal. In the TEM images shown in Figure 2c,d, the presence of pores in the porous TiO₂ NPs (denoted hereafter as PT200; Figure 2d) is clearer compared to the solid TiO₂ NPs (denoted hereafter as ST200; Figure 2c). This suggests that a simple aqueous washing for the TiO₂–NaCl composite NPs is effective in removing the salt templates and creating pore structures inside the TiO₂ matrix.

These results were corroborated by the BET measurement of pore-size distribution for the as-prepared solid and porous TiO₂ NPs. The BET surface areas were ~7 m²/g for the ST200 NPs and ~200 m²/g for the PT200 NPs fabricated using the current approach. The BET surface area of the ST25 NPs used as a

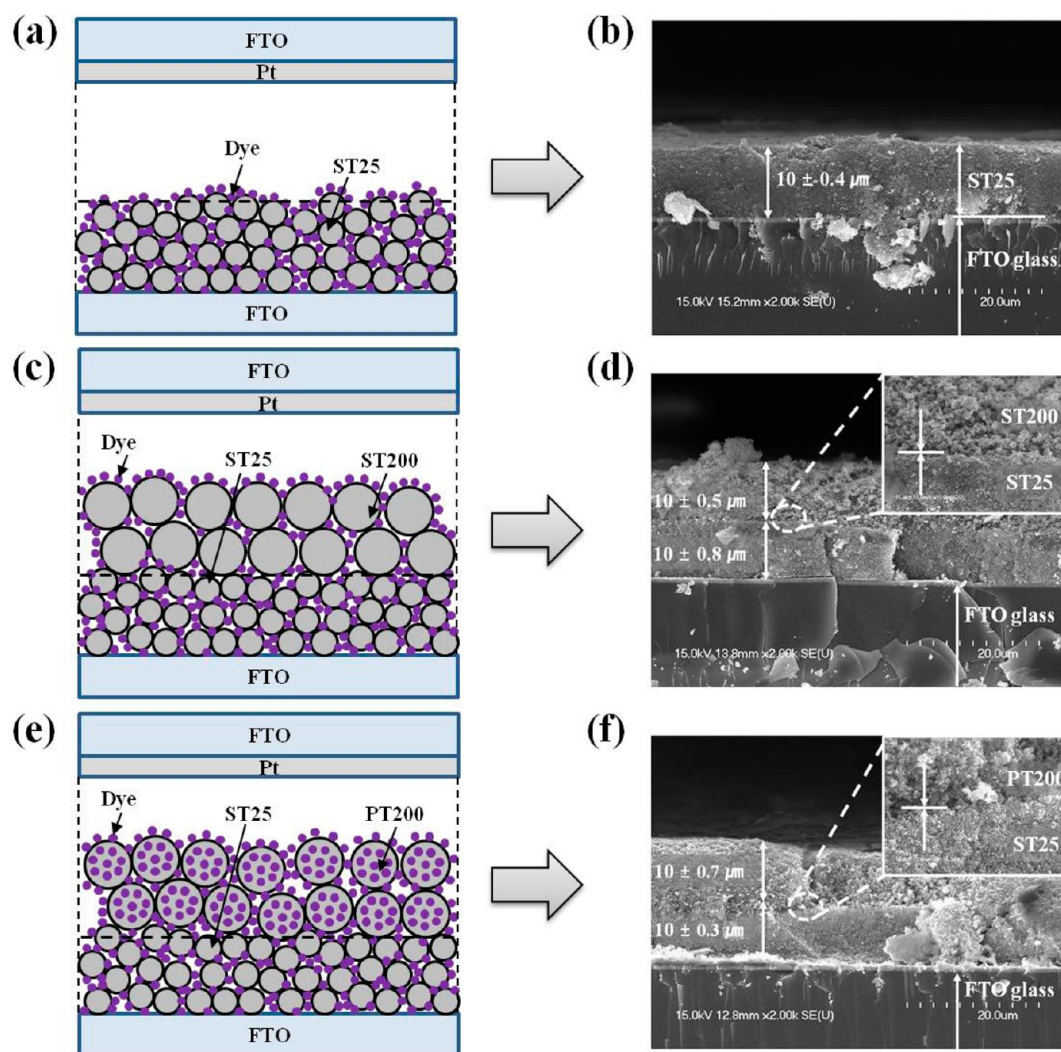


Figure 4. Schematics and cross-sectional SEM images of ST25 SL, ST25/ST200 DL, and ST25/PT200 DL.

reference material was $\sim 50 \text{ m}^2/\text{g}$. Similarly, the adsorption and desorption curves in Figure 3a show that the amount of nitrogen molecules adsorbed were found to increase in the order $\text{PT200} > \text{ST25} > \text{ST200}$ NPs. As shown in Figure 3b, the pore size for the PT200 NPs ranged from 1 to 20 nm, and the average pore size was determined to be ~ 5 nm. However, there were no strong peaks at all in the pore-size distribution of the ST200 NPs. These results clearly suggest that the internal pore structures of the PT200 NPs were created by the aerosol-gel and aqueous-washing processes employed in the current approach. Because the pore-size distributions of the ST25 and ST200 NPs originated primarily from the nitrogen molecule adsorption on the intrasurface of the ST25 and ST200 NPs owing to their solid structures, the average solid particle diameters of the ST25 and ST200 NPs can be calculated to be ~ 28 and ~ 203 nm, respectively, which are very close to the average diameters determined from the SEM images shown in Figure 2a,b. Here, the average diameter of the TiO_2 NPs was calculated by the simplified equation $D_p = 6 \times (\text{SSA}\rho)^{-1}$, where D_p is the average diameter of solid TiO_2 NPs, SSA is the specific surface area determined by BET measurement, and ρ is the particle density of anatase TiO_2 ($\sim 4.3 \text{ g}/\text{cm}^3$). It should be also noted that in the inset of Figure 3b the average pore size of the PT200 NPs decreased slightly from ~ 5 to ~ 4 nm after

calcination at 500°C . However, the average pore size is still sufficiently large to penetrate and adsorb dye molecules with a 1 to 2 nm long crystal triclinic structure.¹⁷

To clarify the various architectures of the TiO_2 NP-accumulated photoelectrode layers, schematic diagrams and the corresponding cross-sectional SEM images of the photoelectrode layers composed of an ST25 single layer (SL), an ST25/ST200 double layer (DL), and an ST25/PT200 DL are presented in Figure 4. As illustrated in Figure 4a,b, an approximately $10 \mu\text{m}$ thick ST25 SL was employed as a dye-molecule-adsorbing platform layer. As shown in Figure 4c–f, the ST200- and PT200-accumulated overlayers, each approximately $10 \mu\text{m}$ thick, were then fabricated on top of the ST25-accumulated underlayer. As shown in the insets of Figure 4d,f, the ST200 and PT200 overlayers seemed to have more porous structures than the ST25 underlayer because of the presence of larger primary NPs, which is thought to enable more efficient transport for liquid electrolytes.

To examine the spectroscopic properties of the ST25 SL, ST25/ST200 DL, and ST25/PT200 DL, UV–vis absorbance and reflectance spectra analyses were performed, and the results are shown in Figure 5. To verify the role of ST200 and PT200 as effective scattering media inside the photoelectrodes, the overall reflectance of the ST25, ST200, PT200 SLs was

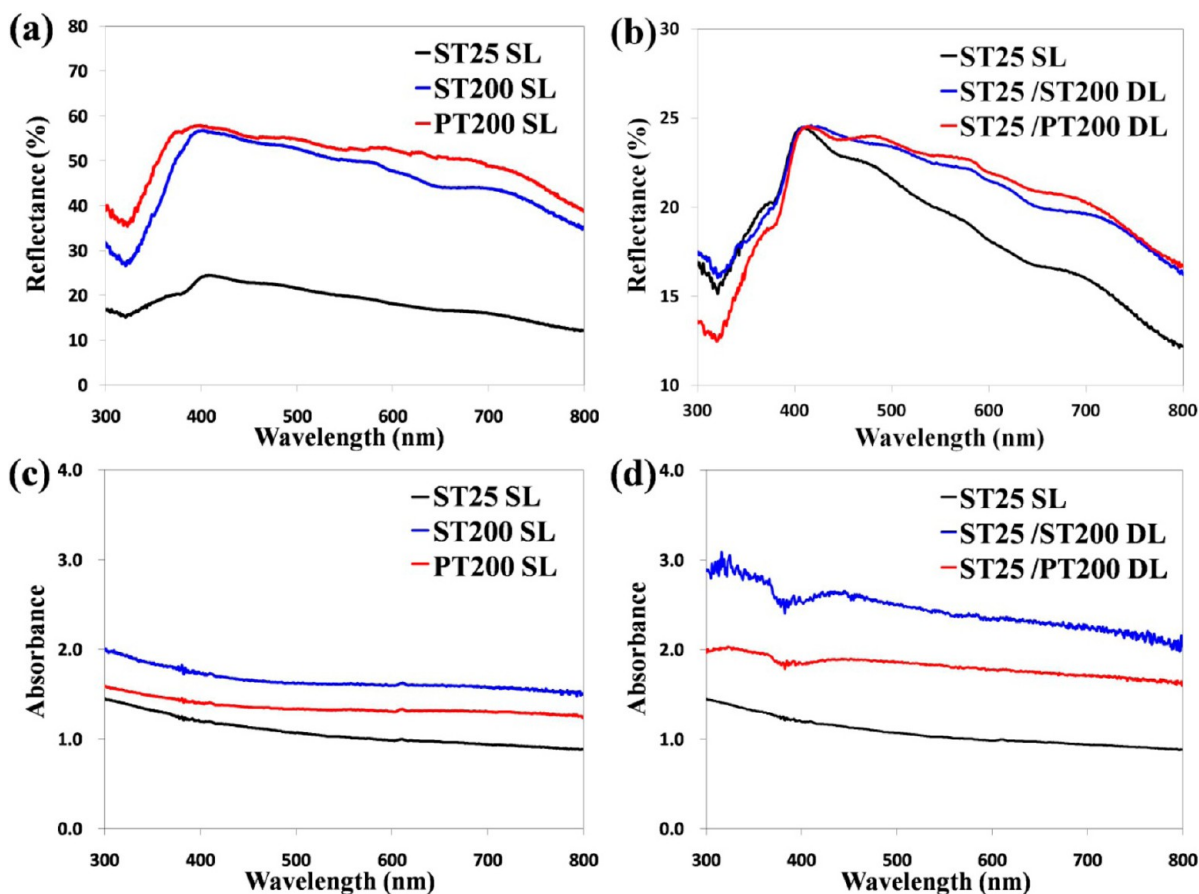


Figure 5. UV–vis reflectance spectra of (a) ST25 SL, ST200 SL, and PT200 SL and (b) ST25 SL, ST25/ST200 DL, and ST25/PT200 DL. UV–vis absorbance spectra of (c) ST25 SL, ST200 SL, and PT200 SL and (d) ST25 SL, ST25/ST200 DL, and ST25/PT200 DL.

Table 1. Summary of the Photovoltaic Characteristics of DSSCs^a

type	τ_e (ms)	M_{DA} (10^{-7} mol cm^{-2})	J_{sc} (mA cm^{-2})	V_{oc} (V)	FF	PCE (%)
ST25 SL	3.06	1.89	6.43 ± 0.09	0.65 ± 0.01	0.72 ± 0.01	2.99 ± 0.16
ST25/ST200 DL	4.00	2.22	6.76 ± 0.21	0.71 ± 0.02	0.75 ± 0.01	3.60 ± 0.11
ST25/PT200 DL	5.03	2.50	8.84 ± 0.52	0.77 ± 0.01	0.72 ± 0.01	5.05 ± 0.13

^aST25 = solid TiO_2 NP with an average diameter of 25 nm, ST200 = solid TiO_2 NP with an average diameter of 200 nm, PT200 = porous TiO_2 NP with an average diameter of 200 nm, SL = single layer, DL = double layer, τ_e = electron lifetime, M_{DA} = amount of dye adsorbed, J_{sc} = short-circuit current, V_{oc} = open-circuit voltage, FF = fill factor, and PCE = power conversion efficiency.

examined first; the results are shown in Figure 5a. As expected, the magnitudes of the reflectance of the ST200 and PT200 SLs were much higher than that of the ST25 SL, suggesting that both the ST200 SL and the PT200 SL are effective light-scattering media in the photoelectrodes. However, when the ST200 and PT200 NPs were accumulated on top of the ST25 NPs (i.e., comparing the ST25 SL, ST25/ST200 DL, and ST25/PT200 DL), the overall reflectance of all of the samples was quite similar with relatively low values, as shown in Figure 5b, implying that the reflected light from the ST200 and PT200 overlayers was mostly absorbed by the ST25 underlayer, resulting in an increase in the amount of light absorbance for the ST25/ST200 and ST25/PT200 DLs as compared to the ST25 SL reference. The intensity of light absorbance was found to increase in the order ST200 SL > PT200 SL > ST25 SL (Figure 5c) and ST25/ST200 DL > ST25/PT200 DL > ST25 SL (Figure 5d). The possible reason for the increased light absorbance in the spectral range of 200–800 nm in the ST25/ST200 and ST25/PT200 DLs as compared to that in the

ST25 SL is that in both ST200 and PT200 the NP-accumulated overlayer played the role of an effective light-scattering medium, which resulted in an increase in the number of light pathways in the photoelectrode. It could be inferred that incorporation of such large particles (i.e., ST200 and PT200 NPs) resulted in significant light-scattering (Mie theory), eventually leading to improved light harvesting in the DLs of the photoelectrodes.

The dark J – V characteristic curves of DSSCs for the ST25/ST200 DL- and ST25/PT200 DL-based photoelectrodes were compared, and the results are shown in Figure 6a. An ST25 SL-based DSSC was provided as a reference cell. The ST25/ST200 DL-based DSSCs exhibited earlier onset and a larger magnitude of the current density than the ST25/PT200 DL-based DSSCs, thus reflecting a higher electron recombination rate in the ST25/ST200 DL than in the ST25/PT200 DL. The lower electron recombination for the ST25/PT200 DL can be attributed to the fact that PT200 NPs play the key role of effective transfer medium for photogenerated electrons because of the presence of internal pore structures.

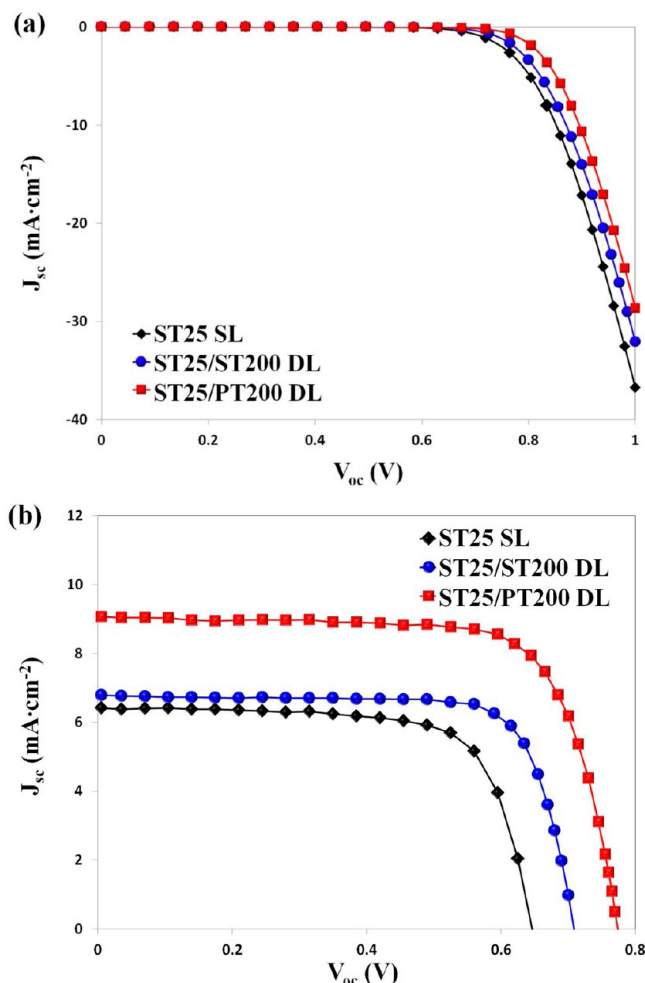


Figure 6. (a) Dark J - V curves of ST25 SL, ST25/ST200 DL, and ST25/PT200 DL. (b) J - V curves of ST25 SL, ST25/ST200 DL, and ST25/PT200 DL.

Table 1 and Figure 6b summarize the photovoltaic characteristics and J - V curves of the fabricated DSSCs measured under AM 1.5 illumination ($100 \text{ mW}/\text{cm}^2$). The ST25 SL-based DSSC had a J_{sc} and PCE of $6.43 \pm 0.09 \text{ mA}/\text{cm}^2$ and $2.99 \pm 0.16\%$, respectively. By adding the ST200 NP-accumulated overlayer on top of the ST25 SL underlayer (i.e., the ST25/ST200 DL-based DSSC), the J_{sc} and PCE increased to $6.76 \pm 0.21 \text{ mA}/\text{cm}^2$ and $3.60 \pm 0.11\%$, respectively, because of the enhanced light-scattering effect of the ST200 NPs. However, the ST25/PT200 DL-based DSSC had much higher J_{sc} and PCE values of $8.84 \pm 0.52 \text{ mA}/\text{cm}^2$ and $5.05 \pm 0.13\%$, respectively. The PCE value of the ST25/PT200 DL-based DSSC was 169 and 140% compared to that of the ST25 SL- and ST25/ST200 DL-based DSSCs, respectively. This can be attributed to the synergistic effect of both the effective dye adsorption and enhanced light harvesting, which occurred simultaneously because of the internal pore structure and light-interfering size of the PT200 NPs. The PT200 NP-accumulated overlayer had a much higher specific surface area because of the presence of internal pore structures, enabling them to support many dye molecules compared to the ST200 NP-accumulated overlayer; hence, the number of photogenerated electrons was significantly increased.

To find a direct evidence for this hypothesis, we examined the amount of dye adsorption using UV-vis spectrometry after

dissolving the dye molecules adsorbed in the photoelectrodes with a NaOH solution. The dye adsorption was found to be $\sim 1.89 \times 10^{-7} \text{ mol g}^{-1}$ for the ST25 SL, $\sim 2.20 \times 10^{-7} \text{ mol g}^{-1}$ for the ST25/ST200 DL, and $\sim 2.50 \times 10^{-7} \text{ mol g}^{-1}$ for the ST25/PT200 DL. Also, as noted in Table 1, the V_{oc} of the ST25/PT200 DL-based DSSC (i.e., $V_{oc} = 0.77 \pm 0.01 \text{ V}$) was much larger than that of the ST25 SL- and ST25/ST200 DL-based DSSCs (i.e., $V_{oc} = 0.65 \pm 0.01$ and $0.71 \pm 0.01 \text{ V}$, respectively). These results are thought to be because V_{oc} is inversely proportional to the charge recombination rate, as shown in eq 1.¹⁹

$$V_{oc} = \frac{kT}{q} \ln\left(\frac{I_{inj}}{I_0} + 1\right) \quad (1)$$

where k is the Boltzmann constant, T is the absolute temperature, q is the magnitude of the electron charge, I_{inj} is the concentration of electrons injected to the TiO_2 , and I_0 is the dark current (i.e., $I_0 = qn_0k_{et}[I_3^-]$, where n_0 is the electron density of the conduction band of the TiO_2 in the dark, k_{et} is the rate constant for recombination, and $[I_3^-]$ is the concentration of the oxidized redox mediator in the liquid electrolyte). Therefore, the increase in the V_{oc} of the ST25/PT200 DL-based DSSC resulted from the lower charge recombination rate and the higher concentration of the electrons injected into the TiO_2 .

To understand the major factor responsible for the improved PCE for the ST25/PT200 DL-based DSSCs, the incident photon-to-electron conversion efficiency (IPCE) spectra were measured as a function of the incident-light wavelength. The IPCE spectra, shown in Figure 7, show that the ST25/PT200

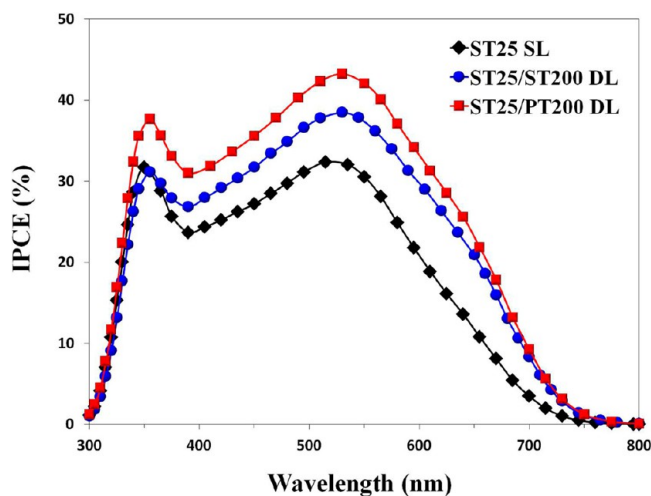


Figure 7. IPCE spectra of DSSCs with ST25 SL, ST25/ST200 DL, and ST25/PT200 DL.

DL-based DSSCs exhibited a better IPCE than the ST25 SL- and ST25/ST200 DL-based DSSCs, suggesting that the PT200 NPs can provide a more effective light-harvesting capacity than the ST200 NPs. The relative magnitude of the IPCE spectra for the ST25/PT200 DL-based DSSCs is much higher than that of the ST25/ST200 DL-based DSSCs, confirming that the mesoporous TiO_2 NPs are effective dye-supporting and light-scattering particles that enhance the photovoltaic performance of DSSCs.

Electrochemical impedance spectroscopy (EIS) measurements were also carried out to identify the charge-transfer-related internal resistance of the ST25/ST200- and ST25/PT200 DL-based

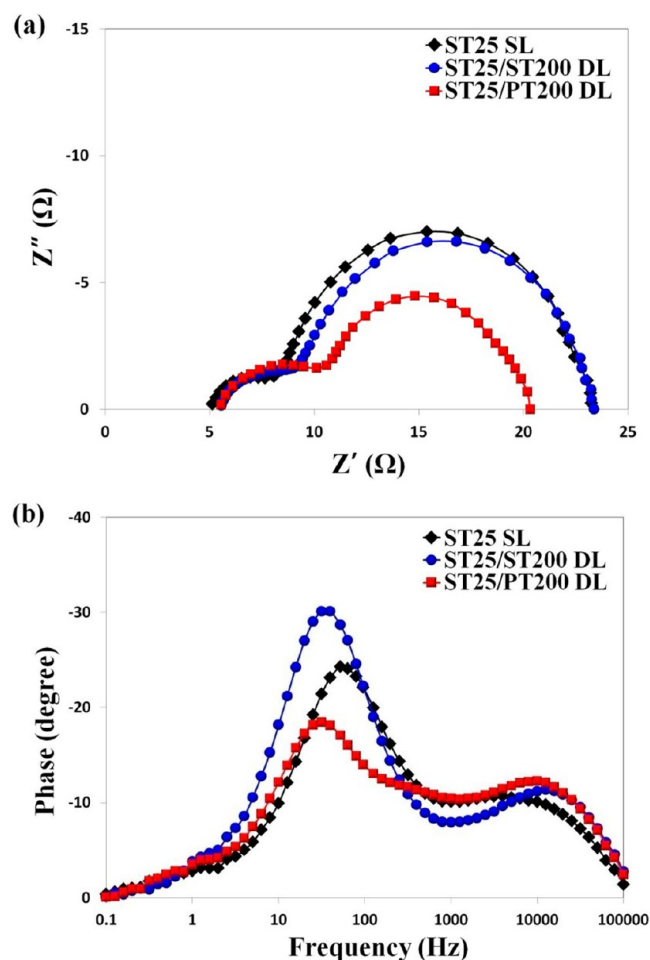


Figure 8. (a) Nyquist plots of ST25 SL, ST25/ST200 DL, and ST25/PT200 DL. (b) Bode plots of ST25 SL, ST25/ST200 DL, and ST25/PT200 DL.

photoelectrodes, as shown in Figure 8. The Nyquist plots in Figure 8a show that the ST25/PT200 DL reduced the charge-transfer resistance at the TiO_2 NP/dye/electrolyte interfaces. The ST25/PT200 DL generated more electrons, which eventually resulted in a lower resistance and higher J_{sc} as shown in Figure 8a and Table 1. Figure 8b shows Bode phase plots for analyzing the electron lifetime. The maximum frequency decreased with the ST200 and PT200 overlayers, and the electron lifetime ($\tau_e = [2\pi f_{max}]^{-1}$, where f_{max} is the maximum frequency²⁰) increased from 3 ms for the ST25 SL-based DSSCs to 4 ms for the ST25/ST200 DL-based DSSCs and 5 ms for the ST25/PT200 DL-based DSSCs, suggesting that the photogenerated electrons diffuse further in the order ST25/PT200 DL > ST25/ST200 DL > ST25 SL.

CONCLUSIONS

In this work, we synthesized solid and mesoporous TiO_2 NPs via inorganic templates for aero-sol-gel and subsequent aqueous-washing processes. After the solid and mesoporous TiO_2 NPs were fabricated, they were used to form a photovoltaic active overlayer ($0.6 \times 0.6 \text{ cm}^2$) on top of an ST25-based platform underlayer in the DSSC photoelectrodes. The capacity of the mesoporous TiO_2 NPs (i.e., PT200) with a relatively high specific surface area and large primary size was systematically examined in terms of their ability to adsorb the dye molecules and to scatter the incident light in the DSSC

photoelectrodes. Compared to the ST25/ST200 DL-based DSSCs, the ST25/PT200 DL-based DSSCs fabricated in this study showed a significant improvement in the J_{sc} and PCE values, increasing from 6.76 ± 0.52 to $8.84 \pm 0.52 \text{ mA cm}^{-2}$ and from 3.60 ± 0.11 to $5.05 \pm 0.13\%$, respectively. These results suggest that a double-layered photoelectrode consisting of small solid TiO_2 NPs (i.e., ST25) and large mesoporous TiO_2 NPs (i.e., PT200) can support a higher concentration of dye molecules and scatter the incident light more effectively, thus improving the light-harvesting capabilities of DSSCs.

AUTHOR INFORMATION

Corresponding Author

*E-mail: sookim@pusan.ac.kr.

Notes

The authors declare no competing financial interest.

ACKNOWLEDGMENTS

This study was supported by the National Research Foundation of Korea (NRF), funded by the Korean government (MEST) (2011-0013114).

REFERENCES

- (1) Grätzel, M. J. *Photochem. Photobiol.*, C **2003**, 4, 145–153.
- (2) Ito, S.; Chen, P.; Comte, P.; Nazeeruddin, M. K.; Liska, P.; Pechy, P.; Grätzel, M. *Prog. Photovoltaics* **2007**, 15, 603–612.
- (3) Zhu, K.; Neale, N. R.; Miedaner, A.; Frank, A. J. *Nano Lett.* **2007**, 7, 69–74.
- (4) Hardin, B. E.; Hoke, E. T.; Armstrong, P. B.; Yum, J.-H.; Comte, P.; Torres, T.; Frechet, J. M. J.; Nazeeruddin, M. K.; Grätzel, M.; McGehee, M. D. *Nat. Photonics* **2009**, 3, 406–411.
- (5) Chiang, Y.-F.; Chen, R.-T.; Shen, P.-S.; Chen, P.; Guo, T.-F. *J. Power Sources* **2013**, 225, 257–262.
- (6) Koo, H. J.; Kim, Y. J.; Lee, Y. H.; Lee, W. I.; Kim, K.; Park, N. G. *Adv. Mater.* **2008**, 20, 195–199.
- (7) Xu, H.; Tao, X.; Wang, D.-T.; Zheng, Y.-Z.; Chen, J.-F. *Electrochim. Acta* **2010**, 55, 2280–2285.
- (8) Wu, W.-Q.; Xu, Y.-F.; Rao, H.-S.; Su, C.-Y.; Kuang, D.-B. *Nanoscale* **2013**, 5, 4362–4369.
- (9) Usami, A. *Chem. Phys. Lett.* **1997**, 277, 105–108.
- (10) Usami, A. *Sol. Energy Mater. Sol. Cells* **1999**, 59, 163–166.
- (11) Vargas, W. E.; Niklasson, G. A. *Sol. Energy Mater. Sol. Cells* **2001**, 69, 147–163.
- (12) Docampo, P.; Guldin, S.; Stefiik, M.; Tiwana, P.; Orilall, M. C.; Hüttner, S.; Sai, H.; Wiesner, U.; Steiner, U.; Snaith, H. J. *Adv. Funct. Mater.* **2010**, 20, 1787–1796.
- (13) Cho, C.-Y.; Moon, J. H. *Adv. Mater.* **2011**, 23, 2971–2975.
- (14) Park, J. T.; Chi, W. S.; Roh, D. K.; Ahn, S. H.; Kim, J. H. *Adv. Funct. Mater.* **2013**, 23, 26–33.
- (15) Kim, S. H.; Liu, B. Y. H.; Zachariah, M. R. *Chem. Mater.* **2002**, 14, 2889–2899.
- (16) Kim, S. H.; Liu, B. Y. H.; Zachariah, M. R. *Langmuir* **2004**, 20, 2523–2526.
- (17) Ahn, J. Y.; Cheon, H. K.; Kim, W. D.; Kang, Y. J.; Kim, J. M.; Lee, D. W.; Cho, C. Y.; Hwang, Y. H.; Park, H. S.; Kang, J. W.; Kim, S. H. *Chem. Eng. J.* **2012**, 188, 216–221.
- (18) Ahn, J. Y.; Kim, J. H.; Moon, K. J.; Kim, J. H.; Lee, C. S.; Kim, M. Y.; Kang, J. W.; Kim, S. H. *Sol. Energy* **2013**, 92, 41–46.
- (19) Tromholt, T.; Katz, E. A.; Hirsch, B.; Vossier, A.; Krebs, F. C. *Appl. Phys. Lett.* **2010**, 96, 073501-1–073501-3.
- (20) Qian, J.; Liu, P.; Xiao, Y.; Jiang, Y.; Cao, Y.; Ai, X.; Yang, H. *Adv. Mater.* **2009**, 21, 3663–3667.